Dalton Transactions

ROYAL SOCIETY OF CHEMISTRY

PAPER

View Article Online
View Journal | View Issue

Check for updates

Cite this: *Dalton Trans.*, 2024, **53**, 9763

Radical and diradical states of bis(molybdenocene dithiolene) complexes†

Khalil Youssef, Corentin Poidevin, Antoine Vacher, Arnaud Fihey, Yann Le Gal, Thierry Roisnel and Dominique Lorcy *

Received 7th March 2024,
Accepted 16th May 2024

DOI: 10.1039/d4dt00694a

rsc.li/dalton

The synthesis and characterization of two bis(dithiolene) proligands involving heteroatomic linkers such as 1,4-dithiine and dihydro-1,4-disiline between the two protected dithiolene moieties are described. Two bimetallic complexes involving these heteroatomic bridges between two redox active bis(cyclopentadienyl)molybdenum dithiolene moieties have been synthesized and characterized by electrochemistry, spectroelectrochemistry, and their properties rationalized with (TD-)DFT. Cyclic voltammetry experiments show sequential oxidation of the two redox centers with ΔE values between successive one-electron transfers varying according to the nature of the bridge. Depending on the nature of the heteroatomic bridge, the bis-oxidized complexes exhibit either a diradical character with both radicals essentially localized on the metallacycles, or a closed-shell dicationic state.

Introduction

Dithiolene ligands are non-innocent bidentate ligands which have been known for more than sixty years[1] for their use as precursors of various conducting metal bis(dithiolene) complexes of interest for materials science.[2] The synthesis of ditopic dithiolene ligands, *i.e.* two covalently linked dithiolene ligands, is also currently of interest for the elaboration of conducting polymeric materials. For this purpose, the two chelating sites can be connected through a conjugated organic bridge of various lengths as in tetrathiooxalate (tto),[3–5] 1,2,4,5-benzenetetrathiolate (btt),[6–8] or tetrathiafulvalentetrathiolate ($TTFS_4$) (Chart 1a).[9,10] It is worth mentioning that these three ditopic dithiolene ligands present a common parameter, the two dithiolene units are fused to the organic spacer leading to an almost planar overall structure. This conjugated organic bridge might allow for electronic communication between the two coordinated metal ions, an important parameter to enable charge transport within polymeric materials.[11] In order to evidence the electronic communication between two coordinated metal ions, various electroactive bimetallic complexes have been investigated.[12] For instance, with the btt ligand, electronic interplay has been evidenced in several bimetallic complexes by electrochemistry through the occurrence of multi redox systems and by spectroelectrochemistry through the appearance of an intervalence charge transfer (IVCT) band in the near-IR region.[13–17] For example, when the btt ligand is bridging two bis(cyclopentadienyl) molybdenum(IV) moieties, **Mo_2B** in Chart 1b, a sequential oxidation of each electrophore, Cp_2Mo(dithiolene) units, was observed together with the appearance of an IVCT band in the near IR for the mono-oxidized state.[17] Among the ditopic dithiolene ligands used as precursor of bis molybdenocene complexes, the btt ligand led to the strongest interactions between the two electrophores.[17,18] Herein, in order to keep the two metallacycles in close vicinity, we focused on the use of other six

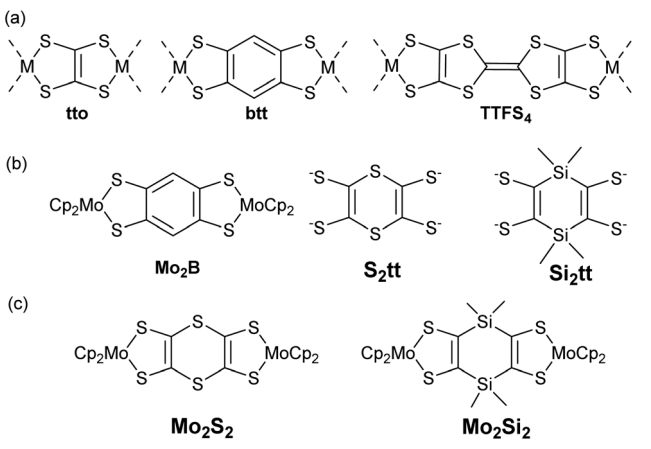

Chart 1 (a) Tetrathiolate ligands involved in linear coordination polymers. (b) **Mo_2B**, 1,4-dithiinetetrathiolate (S_2tt) and dihydro-1,4-disilinetetrathiolate (Si_2tt) ligands. (c) Target bis molydenocene complexes **Mo_2S_2** and **Mo_2Si_2**.

Univ Rennes, CNRS, ISCR (Institut des Sciences Chimiques de Rennes) – UMR 6226, F-35000 Rennes, France. E-mail: dominique.lorcy@univ-rennes1.fr

†Electronic supplementary information (ESI) available: Fig. S1–S23 and Tables S1–S4. CCDC 2333119–2333126. For ESI and crystallographic data in CIF or other electronic format see DOI: https://doi.org/10.1039/d4dt00694a

membered heterocycles that could bring different degree of delocalization relative to the **btt** situation. Thus, we decided to investigate the corresponding 1,4-dithiine and dihydro-1,4-disiline bis(dithiolene) derivatives, **S_2tt** and **Si_2tt** respectively, Chart 1b. These ligands have never been prepared even though theoretical calculations have been performed on coordination polymers involving the **S_2tt** ligand.[19] Heteroatom linkers, such as dithiine or dihydro-1,4-disiline, have been previously used as bridges between electroactive organic molecules such as tetrathiafulvalene (TTF) and they both have shown their efficiency to allow for electronic interplay within the two connected TTFs.[20,21] Therefore we decided to prepare the corresponding ditopic ligands, **S_2tt** and **Si_2tt** (Chart 1b) and to study their propensity to allow for electronic communication within bimetallic complexes, **Mo_2S_2** and **Mo_2Si_2** (Chart 1c). Indeed, Cp_2Mo(dithiolene) complexes are redox active moieties and the heterocyclic linker between the two metallacycles could modulate the nature and the strength of electronic interactions. In this paper we will present a straightforward synthesis of the two novel proligands and the corresponding bimetallic complexes involving two Cp_2Mo(dithiolene) units. Electrochemical and spectrochemical studies have been carried out on the two bimetallic complexes and highlight different behaviors, depending on the nature of the heterocycle. DFT calculations shed light on the comprehension of the possible electronic interactions between the two electrophores depending on the bridge nature.

Results and discussion

Synthesis of the proligands

During the course of our investigations on Cp_2Mo(dithiolene) complexes we found that dithiol-2-one[22] was an excellent dithiolene proligand for the syntheses of such complexes. Therefore, we focused our attention on the preparation of bis(dithiol-2-one) derivatives where the two heterocycles are connected either with a dithiine or a dihydro-1,4-disiline bridging linker. For the dithiine proligand **2**, we did not follow the literature procedure as the overall yield starting from $[Bu_4N][Zn(dmit)_2]$ led to the corresponding dithiine in 2.6% yield only.[23] Instead we developed a novel approach based on the copper catalyzed coupling between aryl iodides and zinc–thiolate complex.[24] Thus, by coupling the 4,5-diiodo-1,3-dithiole-2-thione[25] and the $[Bu_4N][Zn(dmit)_2]$ in the presence of Cu_2O we isolated the sulfur-bridged bis(dithiole-2-thione) **1** in 89% yield (Scheme 1a). This compound is poorly soluble in common organic solvents. Nevertheless, the transchalcogenation of **1** into the bis(dithiol-2-one) **2** was successfully realized by using mercuric acetate in chloroform solution. According to this approach, we isolated the desired proligand **2** in 52% overall yield starting from $[Bu_4N][Zn(dmit)_2]$.

Concerning the synthesis of the dihydro-1,4-disiline bridged bis(dithiolene) proligand **4** we used a similar strategy than the one described in the literature on the tetrathiafulvalene that we adapted for the 1,3-dithiole-2-thione as outlined in Scheme 1b.[21] The bis(metalation) of the 1,3-dithiole-2-thione was realized by adding an excess of LDA and the dilithiated species is further reacted with dichlorodimethylsilane, Me_2SiCl_2. The bis(dithiole-2-thione) **3** was converted into the corresponding dihydro-1,4-disiline bridged bis(dithiole-2-one) **4** by using the procedure described above for the dithiine analogue. It is worthmentioning that the proligand **4** is highly soluble in common organic solvents while the dithiine proligand **2** is less soluble.

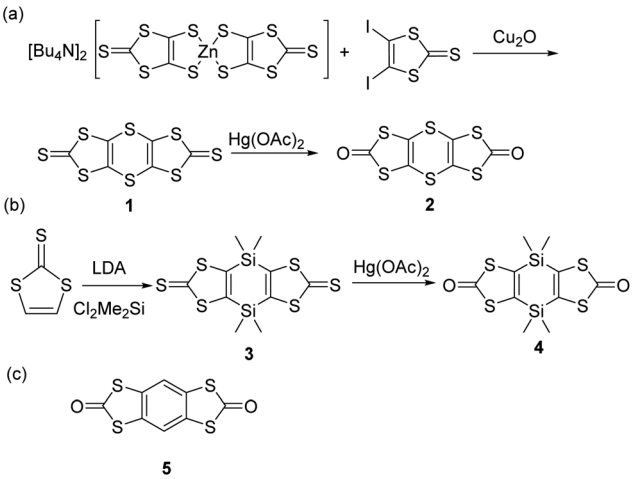

Scheme 1 Synthesis of the proligands **2** and **4**, and molecular structure of **5**.

Crystals were obtained by recrystallization of **2** in $CHCl_3$ and by slow evaporation of a concentrated dichloromethane solution of the derivatives **3** and **4**. For comparison we also recrystallized the known benzo fused bis(dithiol-2-one) **5**[26] into chlorobenzene (Scheme 1c). The molecular structures of the three proligands **2**, **4** and **5** obtained from single X-ray diffraction are given in Fig. 1, the structure of precursor **3** is given in Fig. S1† and bond lengths and selected angles are collected in Table S1 in ESI.† As can be seen in Fig. 1, the dithiine proligand **2** is not planar with a strong folding angle along the S···S hinge of 130°. This value is in the range observed for dithiine subunits which are known to adopt a non-planar conformation (S···S hinge of 127 to 137°)[27,28] and to exhibit clamp-like hinge motions by folding along the S···S axis with an inversion barrier depending on the fused cycles on either side of the 1,4-dithiine cycle from 3 to 7 kcal mol^{-1}.[27–29] Contrariwise, the dihydro-1,4-disiline proligand **4** and the benzo-fused proligand **5** are fully planar.

Syntheses of the complexes

Having in hands these two new proligands **2** and **4**, where two dithiol-2-one are fused to a six-membered ring, we attempted the formation of the bimetallic complexes through the successive addition of MeONa and bis(cyclopentadienyl) molybdenum dichloride (Cp_2MoCl_2) in the medium (Scheme 2). All these reactions were performed using Schlenck techniques as the expected complexes are presumably easy to oxidize, as observed for the benzo analogue **Mo_2B**.[18b] In all the cases, the

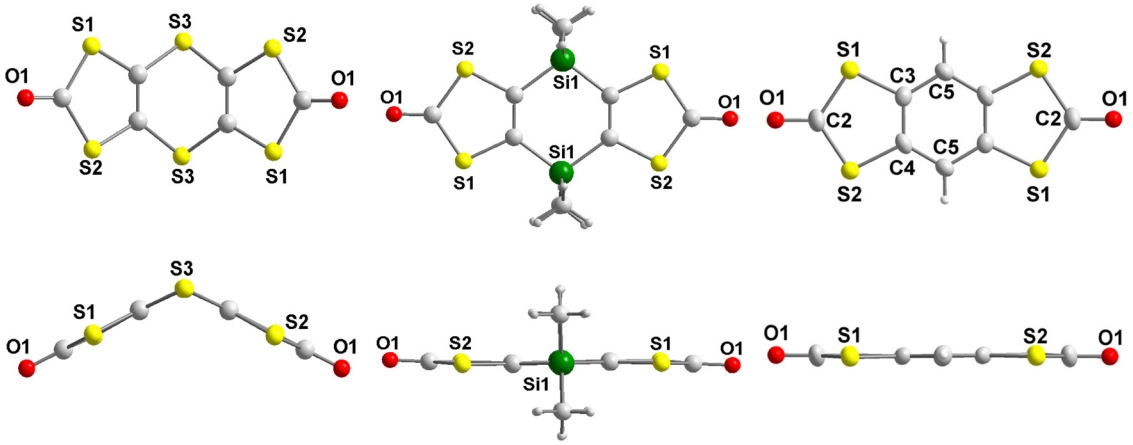

Fig. 1 Top and side views of molecular structures of proligand **2** (left), **4** (middle) and **5** (right).

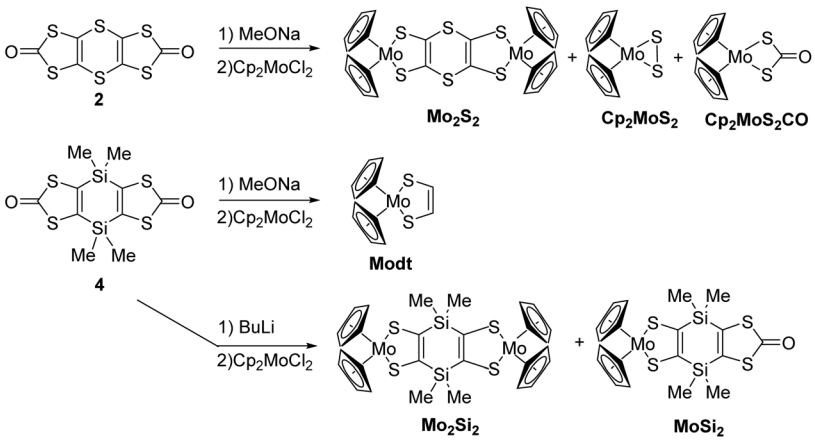

Scheme 2 Synthesis of the metallocene complexes Mo_2S_2, **Modt**, $MoSi_2$ and Mo_2Si_2.

colourless medium of the proligands turned darkly coloured after the addition of base followed by the one of Cp_2MoCl_2. With the dithiine fused bis(dithiolene), we isolated the bis-substituted complex, $\mathbf{Mo_2S_2}$, a poorly soluble complex in common organic solvents, together with more soluble byproducts which were identified by X-ray diffraction studies as molybdenocene disulfide Cp_2MoS_2 [30] and Cp_2MoS_2CO (Fig. S2 and Table S2 in ESI†). On the other hand, in the case of the dihydro-1,4-disiline proligand **4**, the addition of the two reagents led to the destruction of the heterocyclic ring presumably due to the nucleophilic attack of methanolate on the silicium atoms leading to an opening of the ring. Nevertheless, this approach allowed us to isolate the simplest molybdenocene(dithiolene) complex, **Modt**. This complex has been previously reported but with a different synthetic approach and neither crystal structure or electrochemical properties have been investigated so far for this complex.[31] To reach the desired bimetallic dihydro-1,4-disiline complex, $\mathbf{Mo_2Si_2}$, instead of using MeONa we favoured the use of *n*BuLi to deprotect the dithiolene ligands. Accordingly, $\mathbf{Mo_2Si_2}$ was isolated as a soluble bimetallic complex in 47% yield, and the monometallic complex $\mathbf{MoSi_2}$ was isolated as a side product in 6% yield (Scheme 2).

Crystals of the mononuclear complexes, **Modt** and $\mathbf{MoSi_2}$, were obtained by slow concentration of a dichloromethane solution and the molecular structures, elucidated by X-ray diffraction, are given in Fig. 2 and significant bond lengths

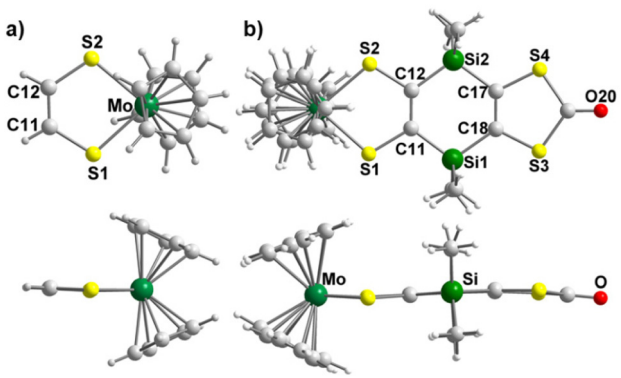

Fig. 2 Molecular structures of **Modt** (a), $\mathbf{MoSi_2}$ (b).

Table 1 Significant bond lengths (Å) and angles (°) of **Modt** and $MoSi_2$

	Modt	$MoSi_2$
C═C	1.327(4)	1.345(5)
C–S	1.749(2)	1.773(3)
	1.753(2)	1.768(3)
S–Mo	2.4513(6)	2.4345(10)
	2.4483(5)	2.4360(8)
S–Mo–S	82.4(1)	82.12(3)

and angles are collected in Table 1. These complexes crystallize in the monoclinic system, space group $P2_1/n$ for **Modt** and $P2_1/c$ for $MoSi_2$. The molecular structure of **Modt** is characterized by a quasi-planar metallacycle (3° along the S···S hinge). Similarly, $MoSi_2$ exhibits a quasi-planar structure with the S···S hinge of the metallacycle reaching 6.3° while within the dithiol-2-one ring the S···S folding angle amounts to 5°.

With now the two desired bimetallic complexes, Mo_2S_2 and Mo_2Si_2 at hand, together with monometallic reference complexes such as **Modt** and $MoSi_2$, we are able to investigate their electronic and optical properties, by comparison with our preliminary results reported with the benzene-centered bimetallic and monometallic complexes, Mo_2B and **MoB** respectively.

Electrochemical studies

Cyclic voltammetry measurements were performed on **Modt**, $MoSi_2$, Mo_2Si_2 and Mo_2S_2 complexes in order to determine their redox properties. The mononuclear complexes, **Modt** and $MoSi_2$, as well as the bimetallic one Mo_2Si_2 were investigated in CH_2Cl_2 and in DMSO for comparison purposes. Concerning Mo_2S_2, it should be mentioned that even in DMSO, this complex is poorly soluble. All the solutions contain 0.1 M of $[Bu_4N][PF_6]$ as supporting electrolyte. The redox potentials are collected in Table 2 together with those previously determined for the benzo analogues **MoB** and Mo_2B,[17] in order to analyze the influence of the heteroatomic bridge on the redox properties.

The cyclic voltammogram (CV) of the mononuclear complexes, **Modt** and $MoSi_2$, investigated in CH_2Cl_2, exhibits two reversible oxidation waves corresponding to the reversible oxidation of the neutral complex into the cation radical species and then to the dication one (Fig. 3). A common feature observed on the CV of the mononuclear complexes studied in DMSO, is that the second oxidation process is not reversible anymore and the oxidation potentials are slightly shifted to higher potentials for the first redox process and to lower oxidation potentials for the second irreversible process. These modifications of the shape of the CV, depending on the solvent used, DMSO *vs.* CH_2Cl_2, are reminiscent of what was previously observed for other mononuclear such as **MoB**. There is a significant influence of the substituent on the metallacycle on the overall donating properties. Indeed, the easiest complex to oxidize is the non-substituted one, **Modt** (+0.09 V *vs.* SCE in CH_2Cl_2), while the most difficult to oxidize is the **MoB** complex with a fused benzo/dithiol-2-one core (+0.42 V *vs.* SCE in CH_2Cl_2) demonstrating the electron withdrawing effect of the fused dithiole-2-one ring in **MoB**.

Table 2 Redox potentials[a] and ΔE_p [b] of the various investigated complexes, *E* in V *vs.* SCE using-$[Bu_4N][PF_6]$

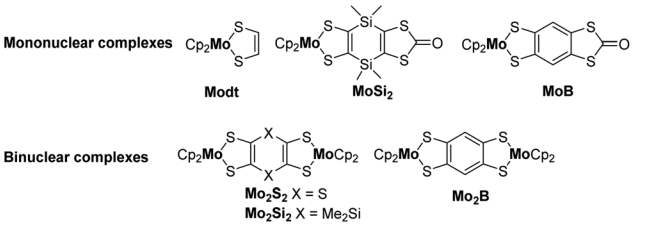

Complexes		$E_{1/2}^1$ (ΔE_p)	$E_{1/2}^2$ (ΔE_p)	$E_{1/2}^3$ (ΔE_p)	$E_{1/2}^4$ (ΔE_p)
Mononuclear	**Modt**	0.09 (70)	0.92 (110)		
(CH_2Cl_2)	$MoSi_2$	0.18 (70)	0.97 (80)		
	MoB	0.42 (70)	1.08 (60)		
(DMSO)	**Modt**	0.13 (70)	0.75*		
	$MoSi_2$	0.24 (70)	0.79*		
	MoB	0.43 (60)	1.01[c]		
Binuclear	Mo_2Si_2	−0.02 (50)	0.21 (60)	0.91	1.08/0.95
(CH_2Cl_2)	Mo_2B	−0.13 (60)	0.37 (60)	1.09 (130)	
	Mo_2Si_2[d]	−0.01 (60)	0.28 (70)	1.38 (90)	—
(DMSO)	Mo_2Si_2	0.06(60)	0.23 (60)	0.79*	
	Mo_2S_2	−0.25 (60)	0.13 (60)		
	Mo_2B	−0.03 (60)	0.38 (70)		
(CH_3CN)	$Mo_2S_2^{2+}$	−0.26 (60)	0.11 (60)	1.00 (60)	
	Mo_2B^{2+}	−0.09(60)	0.34 (60)	1.05 (60)	+1.57

[a] Oxidation processes, taken as the average of the anodic and the cathodic peak potentials. [b] ΔE_p (in mV): peak-to-peak separation. [c] Irreversible process. [d] Using CH_2Cl_2–$[Bu_4N][B(C_6H_4(CF_3)_2)_4]$.

The electrochemical investigation carried out on the bimetallic complex Mo_2S_2 was only performed in DMSO due to solubility issues in CH_2Cl_2. The CV, reported in Fig. 4a, exhibits only two reversible oxidation processes as observed for the bimetallic complex with a benzo linker, Mo_2B, analyzed in the same conditions. Interestingly the presence of the dithiine linker induces a strong cathodic shift of the first redox potential as it occurs at −0.25 V for Mo_2S_2 compared to −0.03 V for Mo_2B (*E* in V *vs.* SCE in DMSO)[17] as well as on the second redox potential (0.13 V for Mo_2S_2 and 0.38 V *vs.* SCE for Mo_2B). It should be noted that due to the narrow potential window of DMSO, no redox processes associated with the dithiin oxidation moiety were observed.[28a] As observed for Mo_2B, and taking to account what was previously observed in the dimeric TTF series, the presence of only two redox processes could be due the small potential window of DMSO. The potential difference between these two redox processes amounts to 380 mV, close to the value noticed for Mo_2B (410 mV).

Concerning the bimetallic complex with the dihydro-1,4-disiline linker, Mo_2Si_2, in dichloromethane, the CV of the Mo_2Si_2 complex displays four oxidation waves (Fig. 4b). The first two waves are reversible and correspond to the oxidation from the neutral state to the radical cation $Mo_2Si_2^{\bullet+}$ and to the dication $Mo_2Si_2^{2+}$. The two other oxidation processes at higher

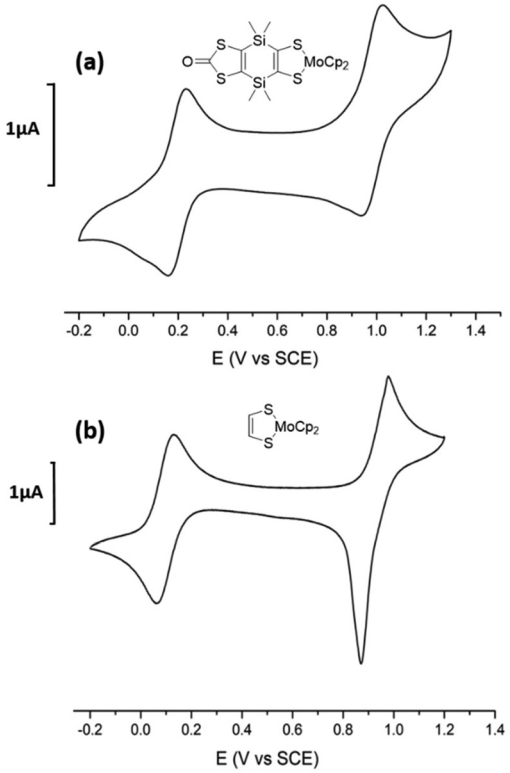

Fig. 3 Cyclic voltammograms of (a) **$MoSi_2$** and (b) **Modt**, in CH_2Cl_2, $[Bu_4N][PF_6]$ 0.1 M (100 mV s^{-1}), *E* in V *vs.* SCE.

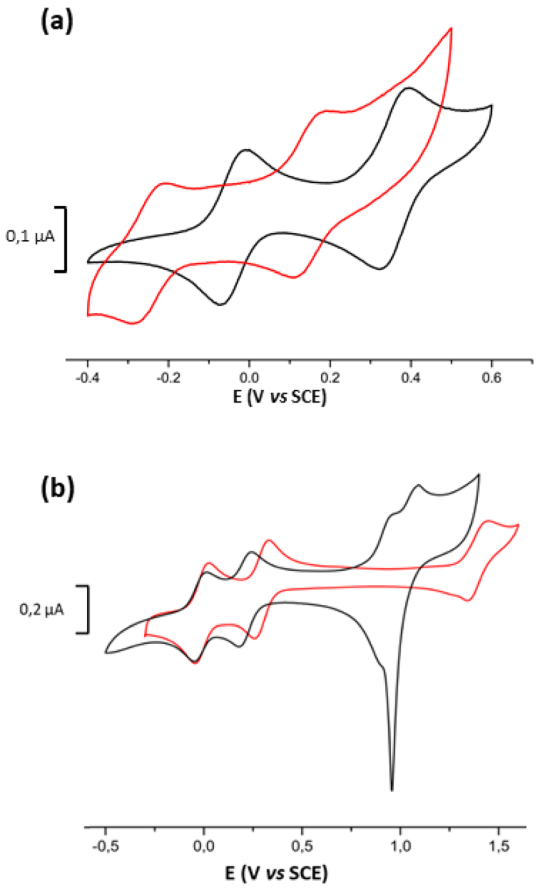

Fig. 4 Cyclic voltammograms of (a) **Mo_2S_2** (red line) and **Mo_2B** (black line) in DMSO, $[Bu_4N][PF_6]$ 0.1 M, (b) **Mo_2Si_2** in CH_2Cl_2 $[Bu_4N][PF_6]$ 0.1 M (black line) and in CH_2Cl_2 $[Bu_4N][B(C_6H_4(CF_3)_2)_4]$ 0.02 M (red line), *E* in V *vs.* SCE, 100 mV s^{-1}.

potentials are no more reversible probably due to adsorption of the oxidized species at the working electrode. These two oxidation waves are assigned to the successive oxidation of **$Mo_2Si_2^{2+}$** into the tricationic state **$Mo_2Si_2^{3+}$** and then to the tetra one **$Mo_2Si_2^{4+}$**. The first redox potential at −0.02 V *vs.* SCE is significantly shifted, by 110 mV, towards higher oxidation potentials compared to the one of **Mo_2B** in the same conditions (−0.13 V *vs.* SCE). Another difference with **Mo_2B**, is the potential difference between the two first redox processes ($\Delta E_{1/2} = E_{1/2}{}^2 - E_{1/2}{}^1$), which amounts to 230 mV for **Mo_2Si_2** while it amounts to 500 mV for **Mo_2B** in CH_2Cl_2. Based on the comparison of CVs obtained in CH_2Cl_2 between **Mo_2Si_2** and **Mo_2B**, the nature of the bridging spacer connecting the two Cp_2Mo(dithiolene) moieties influences significantly the redox activity and the interactions between these two electrophores. Based on the splitting of the two first systems (ΔE), the strength of the interactions between the two electrophores is decreasing from the benzo (500 mV in CH_2Cl_2) to the dihydro-1,4-disiline bridge (230 mV in CH_2Cl_2).

In order to compare the three bimetallic complexes, **Mo_2B**, **Mo_2S_2**, and **Mo_2Si_2**, we also studied the redox behavior of **Mo_2Si_2** in DMSO. At variance with the CV obtained in CH_2Cl_2, the CV of **Mo_2Si_2** realized in DMSO shows clearly the two first redox processes at 0.06 and 0.23 V *vs.* SCE (ΔE = 170 mV) but the third oxidation process can only be distinguished at 0.79 V, at the beginning of the oxidation of the DMSO itself (Fig. S3 in ESI†). Thus, based on the ΔE between the two first redox potentials which amounts to 410 mV for **Mo_2B**, 380 mV for **Mo_2S_2** and 170 mV for **Mo_2Si_2**, the strength of the interactions between the electrophores is decreasing from the benzo to the dithiine and then the weakest one being the dihydro-1,4-disiline bridge.

As previously mentioned,[18] different factors are known to affect the magnitude of the ΔE value between successive one-electron transfers, including electrostatic effects and electronic couplings. Thus, in order to have a more precise idea on the electrostatic contribution in the ΔE values, we investigated the redox behavior of the more soluble **Mo_2Si_2** complex using a weakly coordinating electrolyte CH_2Cl_2–$[Bu_4N][B(C_6H_4(CF_3)_2)_4]$ (or $[Bu_4N][BArF]$).[32] The choice of $[Bu_4N][BArF]$ instead of [Na][BarF] for this study is based on the higher solubility of $[Bu_4N][BArF]$ in CH_2Cl_2 compared to [Na][BArF]. As the [BArF] anion exhibits a very low ion-pairing strength with positively charged species in low polarity solvents such as dichloromethane while solvation dominates in high-polarity solvents such as DMSO, we performed this study only on the **Mo_2Si_2** complex because it is the only well soluble bimetallic complex in dichloromethane.

In the weakly coordinating electrolyte CH_2Cl_2–$[Bu_4N][BArF]$, the CV of $\mathbf{Mo_2Si_2}$ displays three well-resolved reversible processes with similar peak current intensity (Fig. 4b, red line). In these conditions, the potential difference between the first two oxidation waves is slightly affected by the nature of the supporting electrolyte, with a ΔE of 290 mV while it amounts to 230 mV with $[Bu_4N][PF_6]$. The small increase of the ΔE ($E^2 - E^1$) for $\mathbf{Mo_2Si_2}$ (60 mV) indicates a limited electrostatic contribution in the ΔE value. It can be noticed also that the third redox process is significantly anodically shifted as the potential difference between the third and the second redox systems, $\Delta E = E^3 - E^2$, reaches 1.1 V with $[Bu_4N][BArF]$ and only 700 mV with $[Bu_4N][PF_6]$. The increase of this shift indicates that the electrostatic tuning window of the potential differences (ΔE) is larger in the case of the oxidation of already charged species due to the very low ion pairing properties of $[BArF]^-$ in dichloromethane. Using the fluorinated weakly ion pairing anion $[BArF]^-$ as supporting electrolyte, no adsorption at the electrode is observed due to the increased solubility of the polycationic species. Moreover, due to the large anodic shift, the fourth redox system is now located outside the limit of the CH_2Cl_2–$[Bu_4N][B(C_6H_4(CF_3)_2)_4]$ potential window.

Ground state DFT calculations

The optimized geometries of the different oxidation states of $\mathbf{Mo_2S_2}$ and $\mathbf{Mo_2Si_2}$, are reported in Fig. 5. The structure of the neutral $\mathbf{Mo_2S_2}$ is found to be non-planar with a bending angle of 30° (angle taken from mid-points between the three pairs of S atoms from left to right). However, this angle decreases to about 15° to 18° (depending on the structure) for the monocation $\mathbf{Mo_2S_2}^{\bullet+}$ and is close to zero for the dication $\mathbf{Mo_2S_2}^{2+}$. For all oxidation states, several conformers were located within a range of energy of a few kJ mol^{-1}, distinguished by different orientations of the cyclopentadienyl groups. The cation radical, $\mathbf{Mo_2S_2}^{\bullet+}$, has a spin density symmetrically delocalized on both sides of the system as shown on the spin density plot in Fig. 6a. Additionally, this spin density has large contributions on the dithiine linkers. For the di-cationic species, $\mathbf{Mo_2S_2}^{2+}$, as for the benzene linker, $\mathbf{Mo_2B}^{2+}$,[17] the electronic ground state is calculated to be a singlet where the open shell singlet (obtained from a decontaminated broken symmetry solution) is found to be only 0.7 kJ mol^{-1} lower in energy than the closed shell singlet, pointing at a possible coexistence of the two electronic configurations.

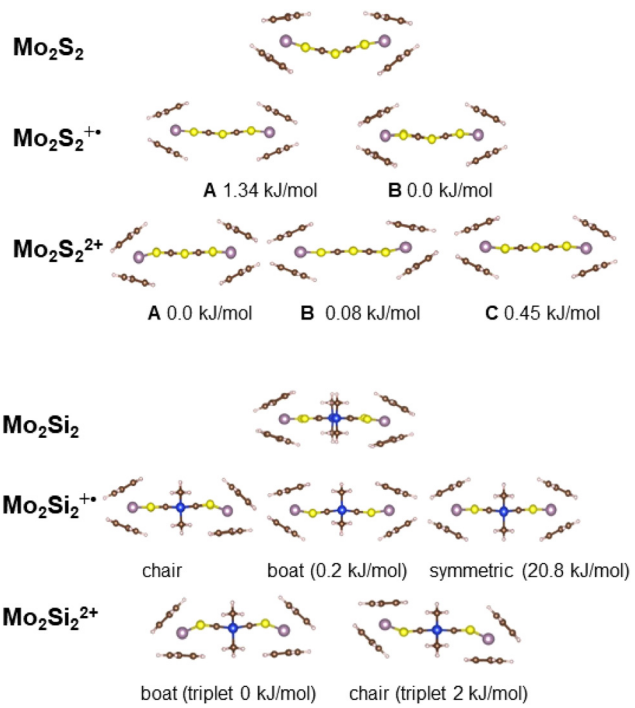

Fig. 5 Representation of the different calculated, low energy conformations of $\mathbf{Mo_2Si_2}$ and $\mathbf{Mo_2S_2}$ and their oxidized species.

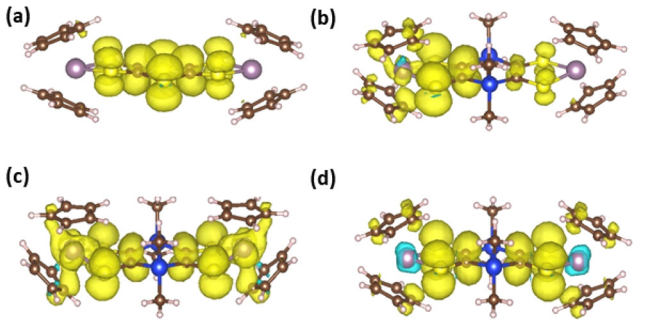

Fig. 6 Spin density plots of (a) $\mathbf{Mo_2S_2}^{\bullet+}$, (b) $\mathbf{Mo_2Si_2}^{\bullet+}$ and (c) $\mathbf{Mo_2Si_2}^{2(\bullet+)}$ (triplet) both in their boat conformation, and (d) symmetric $\mathbf{Mo_2Si_2}^{\bullet+}$ (positive values in yellow and negative values in blue, with an isosurface of 0.001).

Contrary to $\mathbf{Mo_2S_2}$, the structure of the neutral $\mathbf{Mo_2Si_2}$ is found to be planar as can be seen in Fig. 5. The optimized geometries of the oxidized forms, $\mathbf{Mo_2Si_2}^{\bullet+}$ and $\mathbf{Mo_2Si_2}^{2+}$ show the appearance of quasi-degenerate "boat" and "chair" conformations, reminiscent to what was observed for $\mathbf{Mo_2B}^{\bullet+}$ and $\mathbf{Mo_2B}^{2+}$.[17] These structural similarities with $\mathbf{Mo_2B}$ originate from the planar nature of the central ring in both systems. However, the benzene ring induces a conjugated structure between the two dithiolene moieties in $\mathbf{Mo_2B}$ while the absence of π conjugation with the dihydro-1,4-disiline ring in $\mathbf{Mo_2Si_2}$ isolates the two metallocentres. This aspect leads to non-trivial electronic structure in the case of the cation radical species $\mathbf{Mo_2Si_2}^{\bullet+}$ (Fig. 5). Indeed, the geometries of both conformers are computed to be symmetrical (or quasi-symmetrical in the chair conformer) but the radical electron is largely localized on one side of the molecule as can be seen in the spin density plots in Fig. 6b. Upon forcing the system to remain symmetric during the optimization process we did obtain a solution with a spin density delocalized on both side of the molecule (see Fig. 6c). However, this symmetric structure is calculated to be about 20 kJ mol^{-1} higher in energy than the other two previously mentioned. We believe this situation to be the illustration of the limitation of the mono-determinantal nature of the DFT. Another effect of the dihydro-1,4-disiline

bridge compared to the benzene ring is that for the dicationic system, $\mathbf{Mo_2Si_2}^{2+}$, the triplet ground state is calculated to be about 40 kJ mol^{-1} lower in energy than the closed shell singlet. For $\mathbf{Mo_2B}^{2+}$, the triplet was located 18 kJ mol^{-1} higher than the closed shell singlet. Calculations on the broken symmetry solution of $\mathbf{Mo_2B}^{2+}$ at both conformations (boat and chair) showed that an open-shell singlet state was very close in energy to the closed-shell singlet indicating the coexistence of the two electronic configurations. Here, in $\mathbf{Mo_2Si_2}^{2+}$, the decontaminated broken symmetry solution, *i.e.* the open shell singlet solution, is found only 2 kJ mol^{-1} lower in energy than the triplet state. Thus, this theoretical description shows that the electronic ground state of $\mathbf{Mo_2Si_2}^{2+}$ is open shell but it remains difficult to conclude whether it is a triplet or an open shell singlet.

Spectroelectrochemical investigations

In order to determine the UV–vis–NIR spectral signatures of the different redox states, spectroelectrochemical investigations were carried out on the two mononuclear complexes, **Modt** and $\mathbf{MoSi_2}$ as well as on the two binuclear complexes, $\mathbf{Mo_2S_2}$ and $\mathbf{Mo_2Si_2}$. The investigations were carried out on a dichloromethane solution of the most soluble complexes, **Modt**, $\mathbf{MoSi_2}$ and $\mathbf{Mo_2Si_2}$, and in DMSO for both binuclear complexes, $\mathbf{Mo_2S_2}$ and $\mathbf{Mo_2Si_2}$, with 0.2 M $[Bu_4N][PF_6]$ as the supporting electrolyte in all cases.

In dichloromethane the three neutral complexes, **Modt**, $\mathbf{MoSi_2}$ and $\mathbf{Mo_2Si_2}$, exhibit absorption bands only in the UV-vis range with the lowest energy absorption band centered in the range 400 to 600 nm, close to that observed for monometallic[33,34] and bimetallic complexes.[18] This energy band is classically assigned to a ligand–metal charge transfer transition (LMCT) between the dithiolene and the molybdenum. Upon gradual oxidation of the mononuclear complex, **Modt**, besides the modifications in the UV region, the absorption bands initially centered at 518 nm gradually decrease and new absorption bands in the vis-NIR region centered at 660 and 1126 nm grow (Fig. 7a). This evolution upon oxidation is the one typically observed in all the mononuclear Cp_2Mo (dithiolene) complexes with the lowest energy band in the range 1040–1150 nm.[33–35] Then upon oxidation to the dicationic state, $\mathbf{Modt}^{2+}$, a novel absorption band grows centered at 750 nm (Fig. S4†). Similar evolution of the spectra is observed for the $\mathbf{MoSi_2}$ complex, with the signature of the radical cation species in the NIR region at 1150 nm (Fig. 7b).

As the bimetallic complex involving the dithiine linker between the two metallacycles, $\mathbf{Mo_2S_2}$, is easily oxidized in solution, we first reduced the solution to the neutral state through an electrolysis of the solution at −0.4 V *vs.* SCE during 15 min before performing the spectroelectrochemical investigations. Upon gradual oxidation to the monocationic state, $\mathbf{Mo_2S_2}^{\bullet+}$, besides the progressive disappearance of the band localized at 328 nm, new absorption bands in the UV-vis region at 420, 480 nm and in the NIR range at 800, 1154, 1442 nm are growing (Fig. 8a). Then upon oxidation to the second oxidation step, a novel band centered at 855 nm

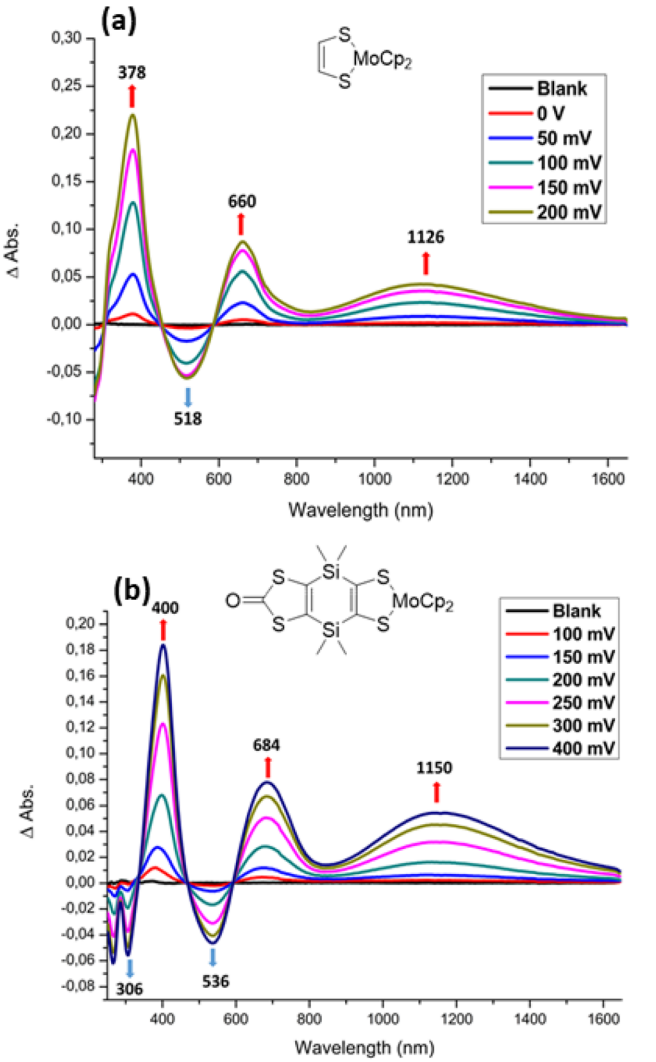

Fig. 7 Differential UV-vis-NIR absorption spectra of the complexes **Modt** (a) and $\mathbf{MoSi_2}$ (b) monitored from neutral state to the monocation radical state upon electrochemical oxidation in CH_2Cl_2–$[Bu_4N][PF_6]$.

increases and the absorption band in the NIR region decreases (Fig. 8b).

The UV-vis-NIR absorption spectra of $\mathbf{Mo_2S_2}$, $\mathbf{Mo_2S_2}^{\bullet+}$, and $\mathbf{Mo_2S_2}^{2+}$ were computed and are shown in Fig. S5 in the ESI.† For the mono-cationic species, despite a broad absorption band in the NIR, several features are missing compared to the experimental differential UV-vis-NIR spectrum (Fig. 8a). As seen before, in the case of $\mathbf{Mo_2B}^{\bullet+}$, such differences can be explained by the inclusion of several conformers.[17] However, this is not the case here as the two conformers A and B of $\mathbf{Mo_2S_2}^{\bullet+}$ give very similar spectral signatures (Fig. S5†). Here, the non-planar structure induced by the dithiine linker can thermally evolve from one orientation to the other. Thus, in this case, instead of using only stable conformers, the dynamical evolution of the structure should be considered to improve the description of the absorption spectra. Molecular dynamics on the three charge states of $\mathbf{Mo_2S_2}$ were performed and a

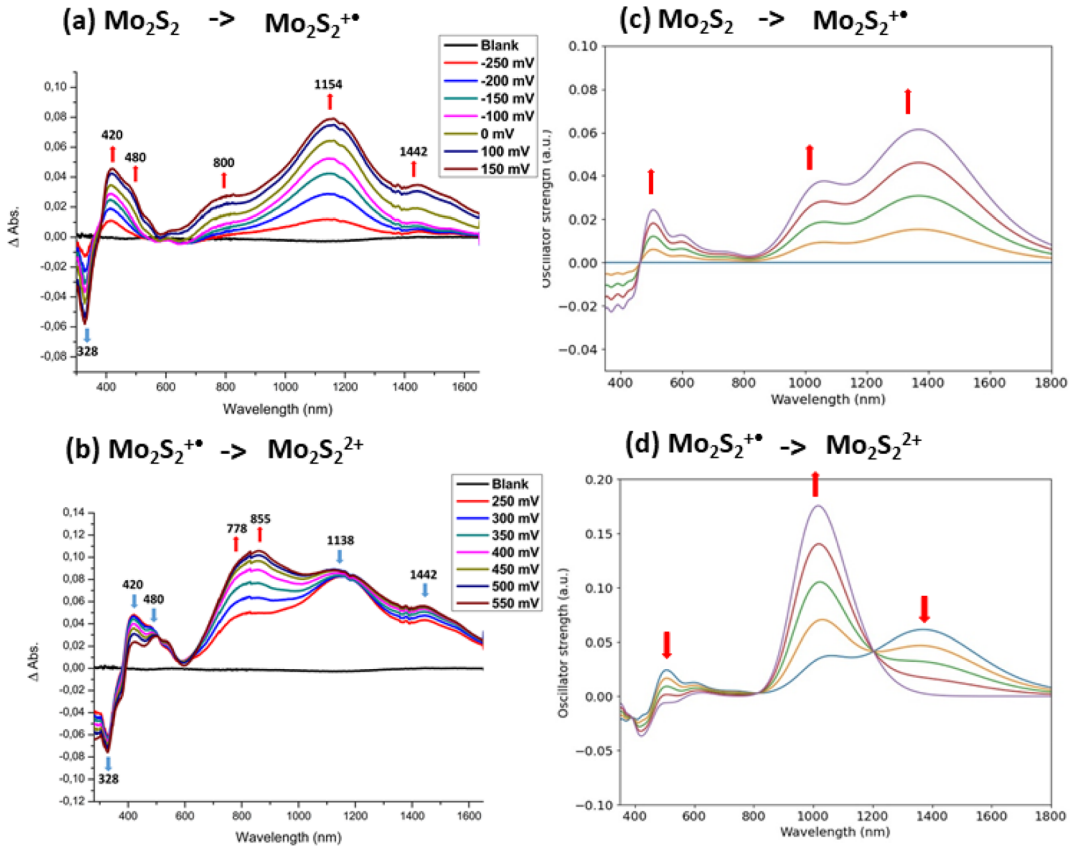

Fig. 8 Experimental (a and b) and simulated (c and d) differential UV-vis-NIR absorption spectra of Mo_2S_2, monitored from neutral to radical cation state (a and c), from radical cation to dication state (b and d), calculated using 50 snapshots of a molecular dynamic simulation (see computational details).

sample of 50 snapshots of each dynamic simulation was selected to generate the averaged UV-vis-NIR spectra (see computational details). The resulting differential UV-vis-NIR spectra are presented in Fig. 8c and d. The calculated differential UV-vis-NIR from neutral $\mathbf{Mo_2S_2}$ to monocation $\mathbf{Mo_2S_2}^{\bullet+}$ now reproduce most of the experimental features with a small red shift, namely a large absorption band at about 1400 nm and a smaller one at around 1050 nm. It appears that the absorption band at about 1050 correspond to structures with the spin localized on one side of the molecule (see spin density in Fig. 9) while the band at about 1400 nm has a spin density delocalised on both sides similar to that of the ground state. The nature of the low energy transitions differs and is identified for the band at 1050 nm as a complete charge transfer between the two sides of the molecule due to the breaking of the symmetry in this conformation, while the latter at 1400 nm exhibits a charge transfer in a symmetric fashion from the S atoms bound to the metal toward the central bridging S atoms (see representations in Fig. 9). Finally, the calculated differential UV-vis-NIR spectra from the monocation $\mathbf{Mo_2S_2}^{\bullet+}$ to the dication $\mathbf{Mo_2S_2}^{2+}$ reproduce well the growth of the experimental band at about 800 nm, albeit from a red shifted to *ca.* 1000 nm, and correspond mostly to a charge

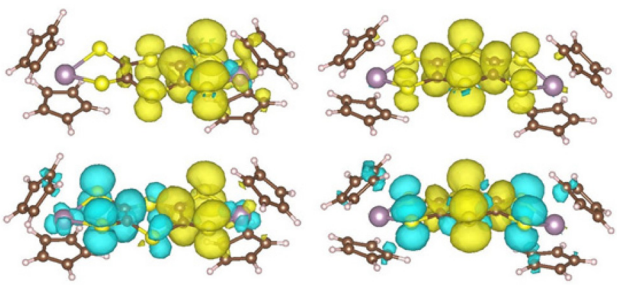

Fig. 9 Characteristic spin densities (top) and charge density difference plots of the first excited state (bottom) of $Mo_2S_2^{\bullet+}$ for snapshots absorbing around 1050 nm (left) and 1400 nm (right) (positive values in yellow and negative values in blue, with an isosurface of 0.001).

transfer from the lateral S atoms to the bridging S atoms (see Fig. S5†).

Upon gradual oxidation of the bimetallic complex $\mathbf{Mo_2Si_2}$ from the neutral to the monocationic state (Fig. 10a), several modifications occur on the spectra in the UV-vis region such as the decrease of the LMCT band at 570 nm and the growth of two new absorption bands at 402 and 724 nm. Moreover, a

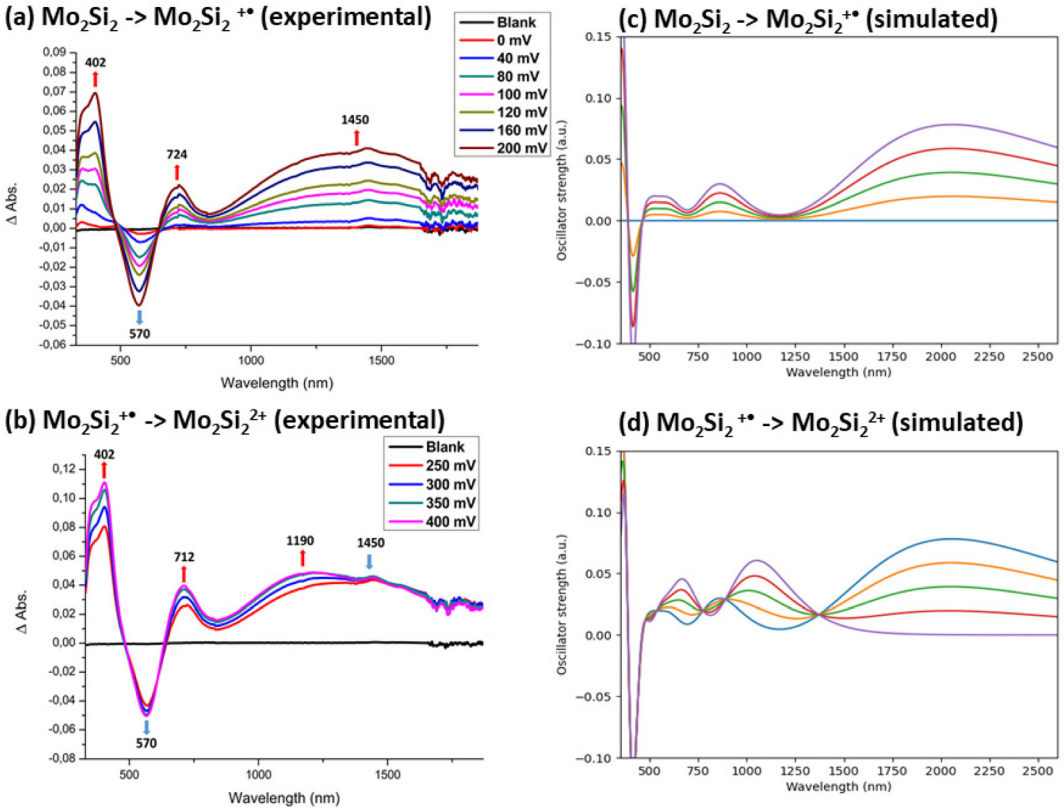

Fig. 10 Experimental (a and b) and simulated (c and d) differential UV–vis–NIR absorption spectra Mo_2Si_2 monitored from neutral to radical cation state (a and c), from radical cation to dication state (b and d).

broad absorption band in the NIR region at 1450 nm is growing (Fig. 10a). The main difference with the mononuclear complex $MoSi_2^{\bullet+}$ (Fig. 7b) is that this absorption is located at lower energy for $Mo_2Si_2^{\bullet+}$ (1450 nm) compared to the one at 1150 nm for $MoSi_2^{\bullet+}$. Gradual oxidation of the mono-oxidized complex $Mo_2Si_2^{\bullet+}$, to the bis-oxidized one, $Mo_2Si_2^{2+}$, induces the growing of a new absorption band at higher energy centered at 1190 nm (Fig. 10b). Interestingly, this spectral signature, especially the wavelength of this absorption band is now observed at an energy similar to the one observed for all the mononuclear complexes under the cation radical state (Fig. 7),[31–33] suggesting that the dicationic state could be ascribed as two, essentially non interacting, radical cation sites.

The theoretical differential UV-vis-NIR absorption spectra between Mo_2Si_2 and $Mo_2Si_2^{\bullet+}$ (Fig. 10c) and $Mo_2Si_2^{\bullet+}$ and $Mo_2Si_2^{2+}$ (Fig. 10d) were computed by artificially increasing the contributions of the oxidized species by 25 percent for each curve. In addition, the separated absorption spectra of the three states are presented in Fig. S6.† The calculated spectrum of $Mo_2Si_2^{\bullet+}$ shows the contribution of three conformers, *i.e.* the two low energy conformers (boat and chair), which are responsible for the absorption band at about 900 nm, together with a broad band centered at 2100 which is due to the symmetric conformer (Fig. S6†). We believe that this symmetric electronic structure is essential to explain the experimental spectrum but it is not well described by DFT and leads to an absorption band largely red shifted. These two types of ground states, localized and symmetric, can be expected to coexist depending on the geometry (dynamical behaviour) and correspond to the broad band starting at 900 nm in the experimental spectrum. The analysis of the transitions reveals a MLCT character for the localized ground state, while for the symmetric ground state the transition corresponds mostly to a charge transfer from Si and S atoms to the bridging carbons and the two metals (see charge density difference plots in Fig. 11). On

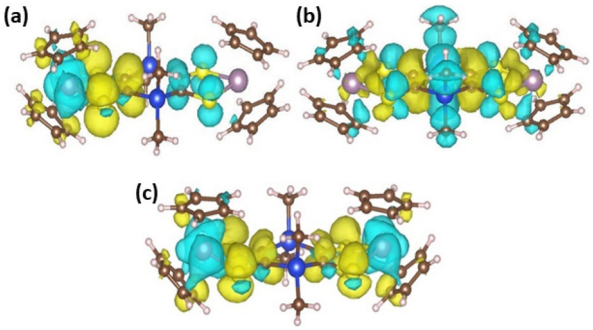

Fig. 11 Charge density difference plot of the first excited state of (a) $Mo_2Si_2^{\bullet+}$ (boat conformer), (b) $Mo_2Si_2^{\bullet+}$ symmetric form and (c) $Mo_2Si_2^{2+}$ (boat conformation) corresponding to the low absorption band around 1100 nm (positive values in yellow and negative values in blue, with an isosurface of 0.001).

the other hand, for $\mathbf{Mo_2Si_2}^{2+}$, the two main bands at *ca.* 700 nm and 1100 nm are well reproduced at this level of theory. The nature of the low energy bands corresponds to a MLCT as can be seen from the charge density difference plot in Fig. 11c. Note that dynamical protocol was also tested for $\mathbf{Mo_2Si_2}$ but did not lead to the low energy band corresponding to the symmetric conformer. Nonetheless, in every case, we underline that the complexity of the experimental spectra can only be understood when considering several conformers with characteristic spin localisation.

Spectral analysis of the chemically oxidized species

In order to bring some experimental support to these calculations for the oxidized species, we attempted to isolate the mono and dicationic complexes derived from $\mathbf{Mo_2S_2}$ and $\mathbf{Mo_2Si_2}$. We performed a chemical oxidation of $\mathbf{Mo_2S_2}$ using two different approaches. We first succeeded in isolating the mono-oxidized species $\mathbf{Mo_2S_2}^{\bullet+}$ after oxidation of the neutral complex with one equivalent of [Fc][BF_4] in CH_2Cl_2. The UV-vis-NIR spectrum in DMSO (Fig. S7a†), shows a band in the NIR region at 1150 nm, which corresponds to the formation of $\mathbf{Mo_2S_2}^{\bullet+}$ as observed during the spectroelectrochemical investigation after oxidation of the neutral complex $\mathbf{Mo_2S_2}$ to the mono-oxidized one $\mathbf{Mo_2S_2}^{\bullet+}$ (see Fig. 8a). We also oxidized the $\mathbf{Mo_2S_2}$ complex in H_2SO_4 in air. Then this solution is poured into an aqueous solution of KPF_6 affording a dark purple precipitate. A part of this precipitate is soluble in acetonitrile and the UV-vis spectrum of this solution shows that it corresponds to the spectral signature of the dicationic species, deduced from the spectroelectrochemical studies (Fig. 8b), with a band centred at 848 nm $\mathbf{Mo_2S_2}^{2+}$ (Fig. S7b†). As the dicationic salt is soluble in CH_3CN we studied the redox behavior at higher potentials by cyclic voltammetry. Following the two redox processes at −0.26 and 0.11 V, associated with the successive oxidation of the complex from 0/+1 and +1/+2, another redox process can now be observed at higher potentials at +1.0 V *vs.* SCE. The EPR of this oxidized species, $\mathbf{Mo_2S_2}^{2+}$, showed no signals associated with the presence of radical species indicating a closed-shell structure. These results are not only consistent with the spectroelectrochemical studies, but also to the theoretical calculations on the $\mathbf{Mo_2S_2}$ complex for the formation of a closed shell singlet in the bis-oxidized complex $\mathbf{Mo_2S_2}^{2+}$.

The chemical oxidation of the more soluble $\mathbf{Mo_2Si_2}$ was performed with one or two equivalents of [Fc][BF_4] in CH_2Cl_2. With only one equivalent of [Fc][BF_4], the color of the solution changed to brown and after 1 h of stirring the addition of petroleum ether to the solution induced the formation of a precipitate. The UV-vis-NIR spectrum of this precipitate in a DMSO solution shows a broad band at 1240 nm together with a band at 500 nm (Fig. S8a†). The shape of this spectrum corresponds to the spectral signature of the mono-oxidized species, $\mathbf{Mo_2Si_2}^{\bullet+}$. Upon addition of 2 equivalents of [Fc][BF_4], the color of the solution changed from purple to green, and a green precipitate appeared in the medium. The UV-vis-NIR spectrum of this precipitate in DMSO or CH_3CN shows a broad band in the NIR region at 1160 nm (Fig. S8b†), which is consistent with the spectrum of the bis-oxidized complex $\mathbf{Mo_2Si_2}^{2+}$ obtained from the spectroelectrochemical experiment (Fig. 10b). It is worthmentioning that the solution of the $\mathbf{Mo_2Si_2}^{2+}$ complex either in CH_3CN or DMSO easily decomposed, even under inert atmosphere. Interestingly, the EPR study carried out on the powder of [$\mathbf{Mo_2Si_2}$][BF_4]$_2$ solubilized in CH_3CN displays on the spectrum a signal at g = 2.0148 in accordance with the presence of an organic radical (Fig. S9†). The absence of any half-field signal around 1600–1700 Gauss in the frozen glass spectrum (66 K) confirms that $\mathbf{Mo_2Si_2}^{2+}$ has a singlet ground state rather than a triplet one. This aligns with the theoretical calculations, indicating the formation of an open-shell singlet state in the bis(oxidized) complex $\mathbf{Mo_2Si_2}^{2+}$ rather than a triplet state.

Conclusions

In summary, we present the synthesis and the characterizations of two bimetallic complexes where two molybdenocene (dithiolene) moieties are fused to a six membered ring. The investigations carried out on these bimetallic complexes allowed us to evidence some striking discrepancies depending on the nature of the central fused six-membered ring: 1,4-dithiine or dihydro-1,4-disiline compared to benzene in the corresponding complexes $\mathbf{Mo_2S_2}$ and $\mathbf{Mo_2Si_2}$ *vs.* $\mathbf{Mo_2B}$. First, the nature of the bridge modifies the overall electron donating ability of these complexes, as the bimetallic complex with the sulfur bridge, $\mathbf{Mo_2S_2}$ oxidizes at the lowest potential, followed by $\mathbf{Mo_2B}$ and $\mathbf{Mo_2Si_2}$. The geometries of these bimetallic complexes are also different, as anticipated from the structural characterization of monometallic complexes and by theoretical calculations. Indeed, the benzene and the dihydro-1,4-disiline bridges lead to planar neutral complexes $\mathbf{Mo_2B}$ and $\mathbf{Mo_2Si_2}$, while the dithiine bridge generates a non-planar, butterfly $\mathbf{Mo_2S_2}$ neutral complex. However, some common features are shared by all three complexes: (i) the two electroactive molybdenocene(dithiolene) moieties oxidize sequentially up to the tetracationic state, (ii) upon gradual oxidation, a broad absorption band in the NIR region corresponding to an IVCT band is observed. Electrochemical and spectro-electrochemical studies reveal that the strongest electronic interaction is observed in $\mathbf{Mo_2B}$, followed by $\mathbf{Mo_2S_2}$ and then $\mathbf{Mo_2Si_2}$. DFT calculations showed that the fused complexes $\mathbf{Mo_2B}$, $\mathbf{Mo_2S_2}$ and $\mathbf{Mo_2Si_2}$ adopt several conformations in their mono- and bis(oxidized) state, which are responsible for their unique NIR absorption properties. Moreover, we show by a combination of DFT calculations and EPR studies of the chemically oxidized complexes that the two fused bis(oxidized) complexes $\mathbf{Mo_2Si_2}^{2(\bullet+)}$ as $\mathbf{Mo_2B}^{2(\bullet+)}$ exhibit a pronounced diradicaloid character while $\mathbf{Mo_2S_2}^{(2+)}$ displays a closed-shell singlet state. The origin of the diradicaloid character in both complexes is different. For $\mathbf{Mo_2B}$, the neutral conjugated structure with the benzene ring evolves upon oxidation towards a non-conjugated one in the bis(oxidized) species while the two non-conjugated electro-

phores in the neutral $\mathbf{Mo_2Si_2}$ stay non conjugated in the bis (oxidized) complex with the dihydro-1,4-disiline junction. Contrariwise, for $\mathbf{Mo_2S_2}$ the antiaromatic connection between the two electrophores in the neutral complex becomes planar and conjugated in the bis(oxidized) complex leading to a closed-shell species.

This work opens the door for a wide variety of future investigations such as the elaboration of other electroactive bi- and trimetallic complexes with different metal ions (Co, Ni, Fe...). These results are also encouraging for the use of these novel ditopic dithiolene ligands for building conducting MOFs, as through-bond and through-space electronic interactions between the electrophores have been evidenced, an important prerequisite for the charge transport within MOFs built out of such ligands.

Experimental section

General

Chemicals and materials from commercial sources were used without further purification. All the reactions were performed under an argon atmosphere. NMR spectra were obtained in $CDCl_3$ unless indicated otherwise. Chemical shifts are reported in ppm, ^{1}H NMR spectra were referenced to residual $CHCl_3$ (7.26 ppm) and ^{13}C NMR spectra were referenced to $CHCl_3$ (77.2 ppm). Melting points were measured on a Kofler hot-stage apparatus and are uncorrected. Mass spectra were recorded by the Centre Régional de Mesures Physiques de l'Ouest, Rennes. Methanol, acetonitrile and dichloromethane were dried using Inert pure solvent column device. Cyclic voltammetry has been performed in a three-electrode cell equipped with a platinum disk working electrode and a glass carbon as counter-electrode. CVs were carried out on a 10^{-3} M solution of complex in CH_2Cl_2 with $[Bu_4][NPF_6]$ 0.1 M. Potentials were measured *versus* Saturated Calomel Electrode (SCE). The spectroelectrochemical setup was performed in CH_2Cl_2–$[NBu_4][PF_6]$ 0.2 M using a Pt grid as the working electrode, a Pt wire as the counter electrode and SCE reference electrode. A Shimadzu 3600 plus spectrophotometer was used to record the UV-vis-NIR spectra. X-band EPR spectra were recorded on a Bruker EMX spectrometer.

Synthesis of bis([1,3]dithiolo)[4,5-*b*:4′,5′-*e*][1,4]dithiine-2,6-dithione 1. $(TBA)_2[Zn(dmit)_2]$ (179 mg, 0.25 mmol), diiodo-1,3-dithiole-2-thione (200 mg, 0.5 mmol), Cu_2O (7.1 mg, 0.05 mmol), ethyl acetoacetate (86 μL, 0.68 mmol), and DMF (3 mL) were placed in a two-necked flask and heated to 80 °C overnight. The orange suspension was cooled down to room temperature and after the addition of 10 mL of CH_2Cl_2, the precipitate was filtered and washed with dichloromethane, water, and diethyl ether, yielding the product as an orange solid in 89% yield (147 mg, 0.44 mmol). Decomposition at 260 °C; HRMS (ASAP) calcd for C_6S_8 $[M^{\bullet+}]$ 327.7760, found 327.7755 (2 ppm).

Synthesis of bis([1,3]dithiolo)[4,5-*b*:4′,5′-*e*][1,4]dithiine-2,6-dione 2. In a 50 mL flask containing bis([1,3]dithiolo)[4,5-*b*:4′,5′-*e*][1,4]dithiine-2,6-dithione **1** (120 mg, 0.36 mmol) in chloroform (20 mL), mercuric acetate (688 mg, 2.16 mmol) was added, and the suspension was stirred overnight at 70 °C. The suspension was filtered over Celite and washed with chloroform. The filtrate was evaporated to afford compound **2** as a yellow solid in 65% yield (70 mg, 0.23 mmol). Crystals of sufficient quality for X-ray diffraction were obtained by recrystallization in hot chloroform. Mp 254 °C; IR: $\tilde{\nu}_{CO}$ = 1681 cm^{-1}; HRMS (ASAP) calcd for C_6S_8 $[M^{\bullet+}]$ 295.8217, found 295.8212 (2 ppm).[24] This compound is not enough soluble in common organic solvents preventing any further characterization.

Synthesis of $\mathbf{Mo_2S_2}$. A solution of NaOMe, freshly prepared from sodium (161 mg, 7 mmol) in 20 mL of dry methanol, was added to a Schlenck tube containing compound **2** (200 mg, 0.67 mmol) in dry THF (20 mL) under an inert atmosphere. Upon the addition of MeONa, the color of the reaction mixture changed from light brown to black suspension. After stirring for 2 h at 45 °C, Cp_2MoCl_2 (398 mg, 1.34 mmol) was added to the medium, and the suspension was stirred overnight at 60 °C. The excess of NaOMe was quenched with water, and most of the solvents were removed under a vacuum. The residue was solubilized in CH_2Cl_2 and the organic phase was washed twice with water. Water was removed *via* cannula and the solvent was removed under vacuum. The precipitate was washed with diethyl ether, then with CH_2Cl_2 to afford $\mathbf{Mo_2S_2}$ as a brown powder in 43% yield (245 mg, 0.35 mmol). Mp > 260 °C, HRMS (MALDI) calcd for $C_{24}H_{20}S_6Mo_2$ $[M^{\bullet+}]$ 695.7991, found 695.805 (8 ppm).

Synthesis of 4,4,8,8-tetramethyl-4,8-dihydro-[1,4]disilino[2,3-*d*:5,6-*d*′]bis([1,3]dithiole)-2,6-dithione 3. To a Schlenck tube containing a solution of 1,3-dithiole (200 mg, 1.5 mmol) in dry THF (20 mL) at −78 °C, a freshly prepared solution of LDA (*n*BuLi 1.6 M solution, 2 mL, 3.2 mmol and diisopropylamine (0.46 mL, 3.3 mmol) in THF 5 mL at 0 °C), was added slowly. After 3 h at −78 °C, Me_2SiCl_2 (0.24 mL, 1.99 mmol) was added, and the temperature was gradually raised to room temperature overnight. The yellow precipitate was collected by filtration, then solubilized in CH_2Cl_2, and the organic layer was washed with water. After drying over $MgSO_4$, the evaporation of the solvent afforded **3** a yellow powder in 56% yield (160 mg, 0.42 mmol). Crystals of sufficient quality for X-ray diffraction were obtained after slow evaporation of a CH_2Cl_2 solution. Mp > 260 °C. ^{1}H NMR (300 MHz, $CDCl_3$) δ 0.55 (s, 12H); ^{13}C NMR (75 MHz, $CDCl_3$) δ 216.4, 152.3, 0.4; HRMS (ASAP) calcd for $C_{10}H_{13}S_6Si_2Mo$ $[M + H]^+$ 380.8874, found 380.8873 (0 ppm); anal. calcd for $[C_{10}H_{12}S_6Si_2{\cdot}0.25\ CH_2Cl_2]$: C, 30.63; H, 3.13 found: C, 30.46; H, 3.47.

Synthesis of 4,4,8,8-tetramethyl-4,8-dihydro-[1,4]disilino[2,3-*d*:5,6-*d*′]bis([1,3]dithiole)-2,6-dione 4. A suspension of compound **3** (150 mg, 0.39 mmol) and $Hg(OAc)_2$ (753 mg, 2.36 mmol) in 15 mL of toluene were stirred under reflux overnight. The suspension was filtered over Celite and washed with dichloromethane. Evaporation of the solvent afforded white precipitate in quantitative yield (135 mg, 0.387 mmol). Crystals of sufficient quality for X-ray diffraction were obtained by slow evaporation of a CH_2Cl_2 solution. Mp 242 °C, ^{1}H NMR

(300 MHz, $CDCl_3$) δ 0.51 (s, 12H); ^{13}C NMR (75 MHz, $CDCl_3$) δ 196.5, 141.1, 0.2; IR: $\tilde{\nu}_{CO}$ = 1646 cm^{-1}; HRMS (ASAP) calcd for $C_{10}H_{12}O_2S_4Si_2$ $[M^{\bullet+}]$ 347.9253, found 347.9250 (1 ppm); anal. calcd for $[C_{10}H_{12}O_2S_4Si_2]$: C, 34.45; H, 3.47, found: C, 34.24; H, 3.49.

Synthesis of Modt. To a two-neck flask containing compound **4** (70 mg, 0.2 mmol) dissolved in dry THF (7 mL) under an inert atmosphere, a solution of NaOMe (freshly prepared from sodium (48 mg, 2 mmol) in 7 mL of dry methanol) was added. The reaction mixture was stirred for 2 h at 45 °C, then the addition of Cp_2MoCl_2 (118 mg, 0.4 mmol), and the suspension was stirred overnight at 60 °C. Evaporation of solvent, then the residue solubilized in CH_2Cl_2. The organic layer was washed with water and dried with $MgSO_4$. After the evaporation of the solvent, a flash column with pure CH_2Cl_2 afforded the product as a purple powder (40 mg, 0.12 mmol) in 31% yield. Crystals of sufficient quality for X-ray diffraction were obtained by slow evaporation of a dichloromethane solution. Mp 260 °C; ^1H NMR (300 MHz, $CDCl_3$) δ 6.21 (s, 2H), 5.25 (s, 10H). ^{13}C NMR (75 MHz, $CDCl_3$) δ 125.4, 97.9. HRMS (ASAP) calcd for $C_{12}H_{13}S_2Mo$ $[M + H]^+$ 318.9507, found 318.9506 (0 ppm); anal. calcd for $[C_{12}H_{12}S_2Mo + 0.2THF]$: C, 46.49; H, 4.15 found: C, 46.68; H, 4.12.

Synthesis of Mo_2Si_2 and $MoSi_2$. To a Schlenck tube containing a solution of compound **4** (200 mg, 0.57 mmol) in dry THF (20 mL) at −78 °C, *n*Buli (1.58 mL, 2.52 mmol) was added slowly and the mixture was stirred for 2 h at −78 °C. After the addition of Cp_2MoCl_2 (340 mg, 1.15 mmol) at −78 °C, the cold bath was removed and the suspension was stirred overnight at room temperature. Addition of dry methanol (25 mL) to the reaction mixture led to the formation of a precipitate which was filtered off. The precipitate was solubilized into CH_2Cl_2 and the organic phase was washed twice with water, and the water was removed *via* cannula. After evaporation of solvents, the precipitate was washed with diethyl ether affording the complex **Mo_2Si_2** as a purple powder in 47% yield (200 mg, 0.27 mmol). Mp > 260 °C; ^1H NMR (400 MHz, DMSO-d_6) δ 5.17 (s, 20H), 0.13 (s, 12H); ^{13}C NMR (101 MHz, DMSO-d_6) δ 147.1, 97.7, 0.2. HRMS (MALDI) calcd for $C_{28}H_{32}Si_2S_4Mo_2$ $[M^{\bullet+}]$ 747.9028, found 747.904 (2 ppm); anal. calcd for $[C_{28}H_{34}OS_4Si_2Mo_2{\cdot}H_2O]$: C, 44.08; H, 4.49; S, 16.81. Found: C, 44.44; H, 4.49; S, 16.10.

$MoSi_2$. The methanol solution was evaporated under vacuum, then the crude product was flash chromatographied on silica gel with pure CH_2Cl_2 to afford **$MoSi_2$** as a red powder in 6% yield. Crystals of sufficient quality for X-ray diffraction were obtained by slow evaporation of a dichloromethane solution. Mp > 260 °C; ^1H NMR (400 MHz, $CDCl_3$) δ 5.15 (s, 10H), 0.37 (s, 12H); ^{13}C NMR (75 MHz, $CDCl_3$) δ 145.03, 143.68, 104.71, 104.56, 97.78, 0.16. HRMS (ASAP) calcd for $C_{19}H_{23}Si_2S_4OMo$ $[M + H]^+$ 548.9218, found 548.9214 (1 ppm).

X-Ray crystallography

Data collections were performed on an APEXII Kappa-CCD (Bruker-AXS) diffractometer equipped with a CCD plate detector for compounds **2**, **3** and **Cp_2MoS_2**, and on a D8 Venture (Bruker-AXS) diffractometer equipped with a CMOS-PHOTON detector for **4**, **5**, **Modt**, **Cp_2MoS_2CO** and **$MoSi_2$** using Mo-Kα radiation (λ = 0.71073 Å, multilayer monochromator). Structures were solved by dual-space algorithm using SHELXT program,[36] and then refined with full-matrix least-squares methods based on F^2 (SHELXL)program.[37] All non-hydrogen atoms were refined with anisotropic atomic displacement parameters. H atoms were finally included in their calculated positions and treated as riding on their parent atom with constrained thermal parameter. Details of the final refinements are summarized in Tables S3 and S4 in ESI. CCDC 2333119–2333126 contain the supplementary crystallographic data for this paper.†

Computational details

All calculations were done using ORCA 5.0 program package.[38] Geometry optimizations were performed at the B3LYP-D3/def2-TZVP level.[39,40] Geometry optimizations were followed by frequency calculations to ensure the validity of the minima. UV-Visible absorption spectra were obtained with TD-DFT calculations at the CAM-B3LYP/def2-TZVP level,[41] computing the first 35 electronic transitions. In addition, RIJCOSX approximations were used to accelerate the SCF procedures.[42] In all steps, solvent (DMSO) effects were included through a Polarizable Continuum Model (PCM). Molecular dynamics calculations were performed using the r2SCAN-3c composite functional with a CPCM model of DMSO, a runtime of 5000 fs and timesteps of 1 fs at 300 K with a Nosé–Hoover chain thermostat.[43]

Conflicts of interest

There is no conflict of interest to declare.

Acknowledgements

Financial support was obtained from ANR (Paris France) under contracts no. 19-CE08-0029-02 and 20-CE09-0002-01, and a PhD grant (to K. Youssef) from Région Bretagne.

References

1 G. Schrauzer and V. P. Mayweg, *J. Am. Chem. Soc.*, 1962, **84**, 3221.
2 (*a*) N. Robertson and L. Cronin, *Coord. Chem. Rev.*, 2002, **227**, 93–127; (*b*) R. Kato, *Chem. Rev.*, 2004, **104**, 5319–5346; (*c*) R. Kato, *Bull. Chem. Soc. Jpn.*, 2014, **87**, 355–374.
3 (*a*) J. R. Reynolds, C. A. Jolly, S. Krichene, P. Cassoux and C. Faulmann, *Synth. Met.*, 1989, **31**, 109–126; (*b*) J. R. Reynolds, F. E. Karasz, C. P. Lillya and J. C. W. Chien, *J. Chem. Soc., Chem. Commun.*, 1985, 268–269; (*c*) J. R. Reynolds, J. C. W. Chien and C. P. Lillya, *Macromolecules*, 1987, **20**, 1184–1191; (*d*) R. Vicente,

J. Ribas, P. Cassoux and L. Valade, *Synth. Met.*, 1986, **13**, 265–280.
4 Y. Sun, L. Qiu, L. Tang, H. Geng, H. Wang, F. Zhang, D. Huang, W. Xu, P. Yue, Y.-S. Guan, F. Jiao, Y. Sun, D. Tang, C. A. Di, Y. Yi and D. Zhu, *Adv. Mater.*, 2016, **28**, 3351–3358.
5 W. Shi, G. Wu, K. Hippalgaonkar, J.-S. Wang, J. Xu and S.-W. Yang, *J. Am. Chem. Soc.*, 2018, **140**, 13200–13204.
6 C. W. Dirk, M. Bousseau, P. H. Barrett, F. Moraes, F. Wudl and A. J. Heeger, *Macromolecules*, 1986, **19**, 266–269.
7 (*a*) C. A. Downes and S. C. Marinescu, *J. Am. Chem. Soc.*, 2015, **137**, 13740–13743; (*b*) C. A. Downes and S. C. Marinescu, *Dalton Trans.*, 2016, **45**, 19311–19321.
8 (*a*) R. Matsuoka, R. Sakamoto, T. Kambe, K. Takada, T. Kusamoto and H. Nishihara, *Chem. Commun.*, 2014, **50**, 8137–8139; (*b*) B. Liu, W. Qiao and Z. Y. Wang, *RSC Adv.*, 2015, **5**, 6815–6822.
9 (*a*) H. Poleschner, W. John, F. G. Hoppe, E. Fanghänel and S. Roth, *J. Prakt. Chem.*, 1983, **325**, 957–975; (*b*) N. M. Rivera, E. M. Engler and R. R. Schumaker, *J. Chem. Soc.*, 1979, **4**, 184–185.
10 (*a*) J. Xie, J.-A. Pan, B. Cheng, T. Ma, A. S. Filatov, S. N. Patel, J. Park, D. V. Talapin and J. S. Anderson, *J. Am. Chem. Soc.*, 2022, **144**, 19026–19037; (*b*) J. Xie, S. Ewing, J. N. Boyn, A. S. Filatov, B. Cheng, T. Ma, G. L. Grocke, N. Zhao, R. Itani, X. Sun, H. Cho, Z. Chen, K. W. Chapman, S. N. Patel, D. V. Talapin, J. Park, D. A. Mazziotti and J. S. Anderson, *Nature*, 2022, **611**, 479–484.
11 S. L. Xie, G. Skorupskii and M. Dincă, *Chem. Rev.*, 2020, **120**, 8536–8580.
12 G. Li, D. Zhu, X. Wang, Z. Su and M. R. Bryce, *Chem. Soc. Rev.*, 2020, **49**, 765–838.
13 L. Chen, M. Wang, F. Gloaguen, D. Zheng, P. Zhang and L. Sun, *Chem. – Eur. J.*, 2012, **18**, 13968–13973.
14 (*a*) H. Köpf and H. Balz, *J. Organomet. Chem.*, 1990, **387**, 77–81; (*b*) H. Balz, H. Köpf and J. Pickardt, *J. Organomet. Chem.*, 1991, **417**, 397–406; (*c*) K. Arumugam, R. Yu, D. Villagrán, T. G. Gray, J. T. Mague and J. P. Donahue, *Inorg. Chem.*, 2008, **47**, 5570–5572; (*d*) K. Arumugam, M. C. Shaw, P. Chandrasekaran, D. Villagrán, T. G. Gray, J. T. Mague and J. P. Donahue, *Inorg. Chem.*, 2009, **48**, 10591–10607.
15 M. Murata, S. Kaji, H. Nishimura, A. Wakamiya and Y. Murata, *Eur. J. Inorg. Chem.*, 2016, 3228–3232.
16 (*a*) M. Nomura and M. Fourmigué, *Inorg. Chem.*, 2008, **47**, 1301–1312; (*b*) B. H. Zhu, Y. Shibata, S. Muratsugu, Y. Yamanoi and H. Nishihara, *Angew. Chem., Int. Ed.*, 2009, **48**, 3858–3861.
17 K. Youssef, C. Poidevin, A. Vacher, Y. Le Gal, O. Charpentier, M. Fourmigué, A. Fihey, F. Barrière, T. Roisnel and D. Lorcy, *Chem. – Eur. J.*, 2023, e202300584.
18 (*a*) A. Vacher, Y. Le Gal, T. Roisnel, V. Dorcet, T. Devic, F. Barrière and D. Lorcy, *Organometallics*, 2019, **38**, 4399–4408; (*b*) K. Youssef, A. Vacher, F. Barrière, T. Roisnel and D. Lorcy, *Polyhedron*, 2022, **226**, 116086; (*c*) N. Bellec, A. Vacher, F. Barrière, Z. Xu, T. Roisnel and D. Lorcy, *Inorg. Chem.*, 2015, **54**(10), 5013–5020.
19 W. Shi, G. Wu, X. Yong, T. Deng, J.-S. Wang, J.-C. Zheng, J. Xu, M. B. Sullivan and S.-W. Yang, *ACS Appl. Mater. Interfaces*, 2018, **10**(41), 35306–35315.
20 (*a*) E. Aqad, J. Y. Becker, J. Bernstein, A. Ellern, V. Khodorkovsky and L. Shapiro, *J. Chem. Soc., Chem. Commun.*, 1994, 2775–2776; (*b*) L. M. Goldenberg, V. Yu, V. Khodorkovsky, J. Y. Becker, M. R. Bryce and M. C. Petty, *J. Mater. Chem.*, 1995, **5**, 191–192.
21 F. Biaso, M. Geoffroy, E. Canadell, P. Auban-Senzier, E. Levillain, M. Fourmigué and N. Avarvari, *Chem. – Eur. J.*, 2007, **13**, 5394–5400.
22 N. Svenstrup and J. Becher, *Synthesis*, 1995, 215–235.
23 H. Yamochi and G. Saito, *Synth. Met.*, 1997, **85**, 1467–1468.
24 J. Sun, X. Lu, J. Shao, Z. Cui, Y. Shao, G. Jiang, W. Yu and X. Shao, *RSC Adv.*, 2013, **3**, 10193–10196.
25 (*a*) R. Gompper, J. Hock, K. Polborn, E. Dormann and H. Winter, *Adv. Mater.*, 1995, **7**, 41–43; (*b*) B. Domercq, T. Devic, M. Fourmigué, P. Auban-Senzier and E. Canadell, *J. Mater. Chem.*, 2001, **11**, 1570–1575.
26 J. Larsen and K. Bechgaard, *J. Org. Chem.*, 1987, **52**, 3285–3288.
27 Z. Lu, H. Liu, X. Lv, W. Lv, Y. Liu and K. Zhu, *Chem. – Eur. J.*, 2023, **29**, e202300101.
28 (*a*) K. Kobayashi and C. L. Gajurel, *J. Sulfur Chem.*, 1986, **7**, 123–148; (*b*) S. I. Etkind and T. M. Swager, *Synthesis*, 2022, **54**, 4843–4863.
29 S. Kim, Y. Kwon, J.-P. Lee, S.-Y. Choi and J. Choo, *J. Mol. Struct.*, 2003, **655**, 451–458.
30 (*a*) A. E. Bruce, M. R. M. Bruce, A. Sclafani and D. R. Tyler, *Organometallics*, 1984, **3**, 1610–1614; (*b*) H. Köpf, S. K. S. Hazari and M. Leitner, *Z. Naturforsch., B: Anorg. Chem., Org. Chem.*, 1978, **33**, 1398–1403.
31 T. Klapötke and H. Köpf, *Z. Anorg. Allg. Chem.*, 1988, **558**, 217–222.
32 (*a*) F. Barrière and W. E. Geiger, *J. Am. Chem. Soc.*, 2006, **128**, 3980–3989; (*b*) W. E. Geiger and F. Barrière, *Acc. Chem. Res.*, 2010, **43**, 1030–1039.
33 J. K. Hsu, C. J. Bonangelino, S. P. Kaiwar, C. M. Boggs, J. C. Fettinger and R. S. Pilato, *Inorg. Chem.*, 1996, **35**, 4743–4751.
34 A. L. Whalley, A. J. Blake, D. Collison, E. S. Davie, H. J. Disley, M. Helliwell, F. E. Mabbs, J. McMaster, C. Wilson and C. D. Garner, *Dalton Trans.*, 2011, **40**, 10457–10472.
35 A. J. Taylor, E. S. Davies, J. A. Weinstein, I. V. Sazanovich, O. V. Bouganov, S. A. Tikhomirov, M. Towrie, J. McMaster and C. D. Garner, *Inorg. Chem.*, 2012, **51**, 13181–13194.
36 G. M. Sheldrick, *Acta Crystallogr., Sect. A: Found. Adv.*, 2015, **71**, 3–8.
37 G. M. Sheldrick, *Acta Crystallogr., Sect. C: Struct. Chem.*, 2015, **71**, 3–8.
38 F. Neese, F. Wennmohs, U. Becker and C. Riplinger, *J. Chem. Phys.*, 2020, **152**, 224108.
39 A. D. Becke, *J. Chem. Phys.*, 1993, **98**, 5648–5652.

40 F. Weigand and R. Ahlrichs, *Phys. Chem. Chem. Phys.*, 2005, **7**, 3297–3305.
41 T. Yanai, D. P. Tew and N. C. Handy, *Chem. Phys. Lett.*, 2004, **393**, 51–57.
42 F. Neese, F. Wennmohs, A. Hansen and U. Becker, *Chem. Phys.*, 2009, **356**, 98–109.
43 S. Grimme, A. Hansen, S. Ehlert and J. M. Mewes, *J. Chem. Phys.*, 2021, **154**, 064103.